PAPER

An integrated molecular–thermodynamic framework for analyzing nanobubbles in supersaturated liquids

Ali Ghamartale,[a] Ehsan Shahini, [ID][a] Aditya Jain,[b] Rogerio Manica, [ID][c] Peter Berg[d] and Tian Tang [ID] *[a]

Nano-sized gas bubbles have attracted significant interest in electro-chemical applications due to their durability and longevity. Accurately predicting nanobubble formation and their size is critical for advancing technologies such as electrolysis and fuel cell systems. This study presents an integrated framework combining molecular dynamics (MD) simulations and thermodynamic modelling to determine nanobubble formation and size in a closed system under isothermal–isobaric condition. Assuming the nanobubble consists of a van der Waals (vdW) gas, the vdW constants are extracted from MD simulations of pure gas systems. A thermodynamic model is then developed for a closed system by combining the vdW equation with the assumption of chemical and mechanical equilibrium, which establishes a predictive relationship between nanobubble size and gas concentration. To validate the framework, MD simulations are performed for hydrogen in water under supersaturation, and the results are compared with thermodynamic model predictions. Comparisons are also made with experimental reports of nanobubbles. Our findings reveal that nanobubbles only form above a critical supersaturation threshold. The framework accurately predicts nanobubble radii in hydrogen–water systems, matching MD results while requiring minimal computational effort. When the pressure inside the nanobubble is approximated from the vdW equation of state, the Young–Laplace equation is shown to be valid even at sub-10 nm scales, with a negligible Tolman length. In contrast, the assumption of an ideal gas in thermodynamic modelling leads to considerable discrepancy with MD simulations. Overall, the proposed approach—bridging MD and thermodynamic modelling—paves the way toward a quantitative understanding of nanobubble formation and size in supersaturated liquids.

1. Introduction

Nanobubble technology has been experiencing a huge growth over the past two decades, emerging as a valuable global market with applications in energy, food, biomedical, and environmental sectors.[1] Nanoscopic bubbles are categorized into surface nanobubbles or bulk nanobubbles,[2] with bulk nanobubbles showing strong potential to enhance processes in various industries.[3] However, despite their positive impact, basic knowledge regarding the formation, stability, size and dynamics of bulk nanobubbles, are still limited, which is the focus of this study.

The International Standard ISO-20480-1-2017 defines nanobubbles as bubbles with a diameter of less than 100 nm that remain suspended in liquid and undergo Brownian motion, unlike larger bubbles that rise to the surface and burst.[4] The exceptional stability and high surface area-to-volume ratio of nanobubbles result in unique properties, such as enhanced gas solubility, which distinguish them from both dissolved molecules and macroscopic bubbles.[1,5,6] Due to their distinctive characteristics, nanobubbles can alter fluid properties resulting in more efficient heat transfer in geothermal systems.[7] They can enhance nutrient permeability in skin care product, leading to effective anti-aging treatments.[8] Of particular interest are hydrogen nanobubbles, which are becoming important in various industries[5] due to their ability to neutralize reactive oxygen species, coupled with high cell penetration and biological compatibility.[9] Hydrogen nanobubbles are typically generated *via* electrochemical methods, such as electrolysis, where hydrogen is produced in hydrogen evolution reactions—found in processes like water splitting—and subsequently forms nanobubbles.[1,10] Understanding bubble properties and dynamics in hydrogen-based applications are crucial for

[a]Department of Mechanical Engineering, University of Alberta, Edmonton, Alberta T6G 1H9, Canada. E-mail: tian.tang@ualberta.ca

[b]Department of Mechanical Engineering, Delhi Technological University, New Delhi, Delhi 110042, India

[c]Department of Mathematical and Statistical Sciences, University of Alberta, Edmonton, Alberta T6G 2G1, Canada

[d]Department of Physics, Brock University, St. Catharines, Ontario L2S 3A1, Canada

optimizing energy use and enhancing process efficiency in such systems.[10]

Classical theories predict that nanobubbles should either collapse or grow once they reach a critical radius.[11] According to the Young–Laplace model, internal pressures in nanobubbles should be exceptionally high (*e.g.*, ~300 atm for a 5 nm radius bubble), leading to rapid dissolution.[1,12] However, experimental observations reveal that nanobubbles can persist for weeks or months under favourable conditions.[13,14] Techniques, such as dynamic light scattering,[2,15] zeta potential analysis,[16] and cryo-electron microscopy,[17] have advanced the understanding of nanobubble behaviour, yet the prediction of their properties such as size and shape continue to be elusive and debated topics. For instance, while some studies attribute nanobubble longevity to charged liquid–gas interfaces and concentration gradients,[12] others emphasize surface polarization independent of bubble charge.[18] Measuring nanobubble size and understanding its dependence on gas supersaturation are unanswered questions in both experimental and computational studies. In addition, bridging molecular view of nanobubbles with their thermodynamic understanding remains a challenge. On this front, some statistical mechanical models have been developed to include molecular interactions into free energy formulations. For example, Yu and Wu[19] proposed a density functional approach that combined the modified fundamental measure theory for hard-sphere interaction with Wertheim's first-order thermodynamic perturbation theory (TPT1) for studying inhomogeneous associating fluids. This framework was applied in Zhou *et al.*[20] to predict the interfacial properties and bubble nucleation of air–water mixtures near a hydrophobic wall. Compared with classical theories, such models are more detailed and capable of predicting non-uniform density distributions of gas and liquid in the system, while requiring more computations.

Molecular dynamics (MD) simulation is another tool used in the literature to study the formation and stability of nanobubbles in liquid. Table 1 provides a detailed review of MD simulations that investigated nanobubbles. In these works, the term 'stable' describes a nanobubble that remains structurally intact and exhibits no spontaneous dissolution over the duration of the MD simulations (tens of nanoseconds), a convention that will also be used to describe nanobubble state in our MD simulations. While providing valuable insights, such as nanobubble size, at the nanoscale,[8] studies listed in Table 1 rarely compared the MD output with thermodynamic modelling to fill the gap of scalability. When a comparison was made in some works, the focus was often on the validity of the Young–Laplace equation, and whether a Tolman correction was needed for the surface tension.[2,12] In the closest effort, Weijs *et al.*[21] attempted to develop a connection between MD simulation and thermodynamics modelling. The modelling was significantly simplified by considering a 2D gas cylinder instead of a 3D gas bubble. A key gap exists in establishing a robust, generalized relationship between the gas supersaturation and the resulting nanobubble size, a connection that has so far been accessible only through MD studies on a case-by-case basis.

In response to this challenge, we propose a streamlined framework to predict nanobubble size by integrating molecular properties of the gas, macroscopic parameters such as surface tension, and thermodynamic conditions. The focus is on bulk nanobubbles, without the presence of a nearby surface. Surface nanobubble is another intriguing topic, with many ongoing studies. For instance, Zhang & Lohse[22] combined MD with a generalized Lohse–Zhang model that considers reaction-driven gas influx and a real-gas (vdW) law, predicting the size evolution and detachment of single electrolytic nanobubbles on nanoelectrodes. Perez Sirkin *et al.*[23] used MD to simulate the nucleation and stationary states of gas bubbles on nano-electrodes, by mimicking electrochemical production of gas at the electrodes. In contrast to these studies, the present work addresses nanobubble formation and size in a closed, non-reactive system under isothermal–isobaric condition. While involving both MD and thermodynamic modelling, our approach does not invoke strict scale separation; rather, we integrate MD outputs with thermodynamic relations calibrated to those outputs.

The rest of the paper is organized as follows: Section 2 describes the theoretical framework including thermodynamic modelling and MD simulation. Section 3 is dedicated to Results and discussion including validation of the framework with MD simulations and experiments. Finally, the conclusion is provided in Section 4.

2. Theoretical framework

The theoretical framework begins by incorporating the vdW equation of state, tuned for the specific gas using MD simulations, into the thermodynamic model (Section 2.1) for a closed system as illustrated in Fig. 1(a). This real-gas treatment parallels recent surface-nanobubble theory at high Laplace pressures.[22] The values of constants in the vdW equation of state are obtained by molecular simulation of pure gas without any liquid (illustrated in Fig. 1(b)), and they reflect the intermolecular interactions that dictate nanobubble behaviour (Section 2.2). Different MD simulations are undertaken to validate the framework, following the methodology described in Section 2.2. A generic picture of the gas-in-liquid simulations is shown in Fig. 1(c) before nanobubble formation and in Fig. 1(d) after nanobubble formation.

2.1. Thermodynamic modelling

Consider a closed system with controlled pressure and temperature, *i.e.*, it operates under the isothermal–isobaric (NPT) condition with prescribed pressure in the liquid P_L (Fig. 1(a)). Mass conservation of the gas implies

$$n_{gT} = n_{gB} + n_{gL}, \tag{1}$$

where n_{gT}, n_{gB} and n_{gL} are respectively the moles of gas in the entire system, in the bubble and dissolved in the liquid, respectively. Denoting the volume of the liquid (excluding the nanobubble) by V_L, the molar concentration of the gas dissolved in the liquid c_{gL} is therefore

Table 1 Summary of MD simulations on bulk nanobubbles. Ensemble defines the thermodynamic condition of the simulation. NVT: canonical ensemble. NPT: isothermal–isobaric ensemble. NVE: microcanonical ensemble. NB: nanobubble

Solvent, forcefield	Gas, forcefield	Concen.^{a} (g L^{-1})	Supersat.^{b}	T (K), P (atm)	Ensemble, MD package	Key findings reported	Ref.
Argon^c	Vacuum	N/A	N/A	99, N/A	NVT, not mentioned	• Stable NBs when the non-dimensional average density is below a critical value of 0.6625 • Simulation domain size significantly impacts NBs instability. Larger domains allow more stable NBs formation • Surface tension of NBs is slightly larger (up to 15%) than that of a planar interface and decreases very slightly with increasing NB size	24
H$_2$O, TIP4P	Vacuum	N/A	N/A	300, N/A	Not mentioned	• Young–Laplace equation is valid for NBs, with small dependency of surface tension on NB size • Threshold radius of unstable NBs is 1 nm, below which NBs shrink and vanish	25
Liquid^c	Gas^c	N/A^d	N/A	300, 1	NPT, not mentioned	• Stable NB when the distance from its periodic image is small (<15 nm) • Larger distances (>30 nm) lead to NB dissolution, unless sufficient gas is present • Equilibrium radius of stable NB matches 2D continuum model predictions, but insufficient gas concentration prevents NB nucleation in simulation, even if predicted to be stable theoretically	21
H$_2$O, SPC/Fw	He, CHARMM	1.085–16.93	713.8–11 138.1	298.15, N/A	NVT-NVE, NAMD	• Preformed NBs below the critical radius of 1 nm are thermodynamically unstable • Inner pressure grows with decreasing radius, resulting in NB instability below the critical radii • Calculated Tolman length is not constant and can be positive or negative depending on the NB size, leading to under- or overestimation of surface tension in some cases	26

Table 1 (Contd.)

| Solvent, forcefield	Gas, forcefield	Concen.[a] (g L⁻¹)	Supersat.[b]	T (K), P (atm)	Ensemble, MD package	Key findings reported	Ref.
H₂O, TIP3P	N₂[c]	13–26	722.2–1444.4	300, 1	NPT, GROMACS	• NBs exhibit a sharp transition from dispersed to assembled states when N₂ concentration exceeds a critical threshold corresponding to supersaturation ≈ 1050 • Density of N₂ inside NB is significantly higher than in the dispersed state and increases as N₂ concentration rises beyond the critical threshold • Formation of NBs occurs within a short time frame (around 20 ns)	27
H₂O, SPC/E	O₂[c]	0.042–35.7	1–850	300, 1	NPT-NVT, LAMMPS	• Stable NBs' radii range from 20 to 400 nm with internal pressure from 120 to 4 atm • Surface tension of water decreases with increasing supersaturation • For high supersaturation (>200), surface tension drops significantly	28
H₂O, CHARMM27	Vacuum	N/A	N/A	300, N/A	NVT, GROMACS	• Stable NB radius range 1.33 to 3.37 nm depending on system size and initial bubble radius • Water surface tension remains nearly constant ($\sim$64.18 mN m⁻¹) regardless of the NB radius • A maximum inter-bubble distance is proposed below which NBs stay stable. The maximum inter-bubble distance $\propto$ (bubble radius)$^{4/3}$	29
H₂O, TIP4P/2005	O₂, N₂[c]	Atomistic: O₂: 21.14–29.17 CG: N₂: 19.41–21.11	O₂: 503.3–694.5 N₂: 1078.33–1172.78	298, 1	NPT, LAMMPS	• Gas molecules of pre-formed NBs exhibit confined diffusion, with most gas molecules (more than 50%) remaining inside the NB over the simulation period • Inner pressures for the NBs are 62.1, 52.3, and 46.9 MPa for bubble radius = 1.88, 2.27, and 2.55 nm, respectively, resulting in ultra-high density inside the NB. • NBs exhibit a double-layer surface charge, with inner layer positively charged and outer layer negatively charged	30

Table 1 (Contd.)

Solvent, forcefield	Gas, forcefield	Concen.[a] (g L⁻¹)	Supersat.[b]	T (K), P (atm)	Ensemble, MD package	Key findings reported	Ref.
H$_2$O, TIP4P/ice, CG[c]	CH$_4$, OPLS-UA, CG[c]	47.13	2142.27	270, 98.7	NPT, GROMACS/LAMMPS	• Young–Laplace equation is valid for pre-formed NBs with radius larger than 5 nm, while smaller NBs are unstable • Minimum center-of-mass distance required to prevent coalescence between two NBs is 20–25 nm, varying slightly with NB size and methane concentration	31
H$_2$O, SPC/E	O$_2$[c]	1.042–13.16	24.81–313.3	293–303, 1	NVT-NPT, LAMMPS	• High supersaturation (>1454.41) supports NB formation by limiting gas diffusion from NB. • Calculated surface tension decreases with supersaturation, averaging 58–68 mN m^{-1} • Elevated temperatures increase gas diffusion and instability	12
H$_2$O, SPC/E	N$_2$[c]	21.01–41.67	1167.2–2315	300, 1	NPT-NVE, LAMMPS	• Small NB (radius = 14 Å) has a high internal pressure (792 atm) and a thicker gas–liquid interface (6.8 Å) compared to large NB (radius = 22 Å, 518 atm, interface thickness 4.4 Å) • Small NB has almost double the diffusion rate of large NB, facilitating faster dissolution • Young–Laplace equation is valid, with surface tension in the range of 55–58 mN m^{-1}, and Henry's law corroborates solubility predictions for different NB sizes	2
Pb–Li eutectic[c]	He[c]	1.62–8.41	N/A	1000, 773.75 as calculate average	NVT, LAMMPS	• NBs exhibit thermodynamic irreversibility when the ratio of gas molecules in the NB to dissolved gas molecules in the liquid respectively, and ρ_L is liquid density. Saturated concentration reported by the National Institute of Standards and Technology (NIST)[33] for N$_2$, O$_2$, CH$_4$ and He are 0.017, 0.042, 0.022, and molecules in the NB to dissolved gas exceeds 0.5, preventing dissolution even under disturbances • Diffusive-shielding effect, driven by background supersaturation, enhances NB formation by reducing gas leakage to the surrounding liquid	32

[a] Unless otherwise specified, mass concentration of the gas (C_{gT}) is calculated from molecular numbers according to $C_{gT} = (N_gM_g)/(N_LM_L/\rho_L)$, where N_g and N_L are number of gas and liquid molecules respectively, M_g and M_L are molecular weight of gas and liquid respectively, and ρ_L is liquid density. [b] Unless otherwise specified, supersaturation = C_{gT}/(saturated concentration) is calculated using column 3 (Concen). Saturated concentration reported by the National Institute of Standards and Technology (NIST)[33] for N$_2$, O$_2$, CH$_4$ and He are 0.017, 0.042, 0.022, and 0.00152 g L^{-1}, respectively. [c] Parameters provided in Table 2. [d] Atomic type and molecular weight not given,[21] N_g = 333–837, N_L = 12 236–52 489.

Table 2 Forcefield parameters in the Lennard-Jones (LJ) potential $U_{LJ}(r_{ij}) = 4\varepsilon_{ij}((\sigma_{ij}/r_{ij})^{12} - (\sigma_{ij}/r_{ij})^6)$, used in MD simulations listed in Table 1. r_{ij} = distance between particles i and j

	ε_{ij} (kcal mol^{-1})	σ_{ij} (Å)	Ref.
Argon	0.240	3.4	24
Liquid	0.717	3.4	21
Gas	0.239	5	21
N of N$_2$	0.069	3.26	27
O of O$_2$	0.095	3.094	12 and 28
O of O$_2$	0.086	3.159	30
N$_2$	0.382	3.6	30
N of N$_2$	0.072	3.32	2
H$_2$O–CH$_4$	Stillinger–Weber potential		31
Helium	Extended Tang–Toennies–Sheng		32
Pb–Li	Embedded-atom method		32
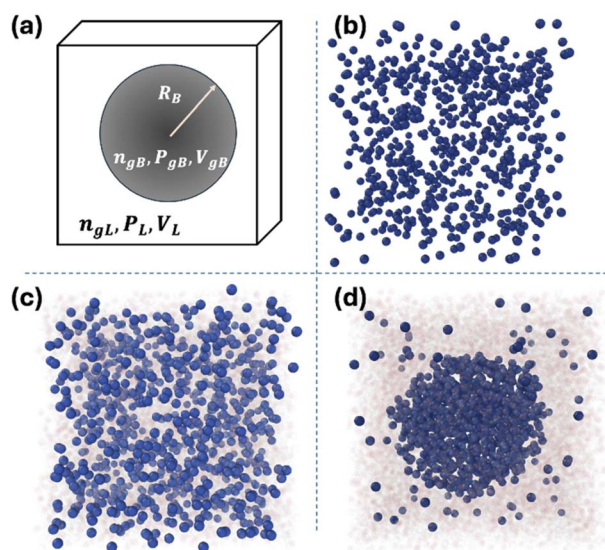
Fig. 1 System design for theoretical modelling and MD simulations: (a) system considered in the thermodynamic modelling with a single gas bubble in liquid, (b) pure gas simulation, (c) initial configuration for gas–liquid systems (gas shown with solid blue circle and liquid shown with a transparent red colour), and (d) gas–liquid systems after a stable nanobubble is formed.

$$c_{gL} = \frac{n_{gL}}{V_L}. \tag{2}$$

c_{gL} can be related to the pressure in the gas bubble (P_{gB}) via Henry's law, $c_{gL} = kP_{gB}$, resulting in

$$n_{gL} = kP_{gB}V_L, \tag{3}$$

where k is the Henry's constant. The substitution of eqn (3) into eqn (1) results in $n_{gT} = n_{gB} + kP_{gB}V_L$. Considering the molecular compositions in the liquid, V_L can be calculated as

$$V_L = (n_{gL}v_{gL} + n_L v_L)N_A, \tag{4}$$

where v_{gL} and v_L are molecular volumes of dissolved gas and liquid, respectively. n_L is mole of liquid and N_A is the Avogadro's

number. While the value of v_L can be straightforwardly determined from experimental density of water, v_{gL} is determined based on the molecular geometry of gas, as $4\pi r_{eff}^3/3$, where r_{eff} is the effective molecular radius (often taken to be the vdW radius). Together,

$$n_{gT} = n_{gB} + kP_{gB}[(n_{gT} - n_{gB})v_{gL} + n_L v_L]N_A. \tag{5}$$

Assuming the gas–liquid interface has a uniform curvature, and the system is free from external forces or dynamic effects, then mechanical equilibrium holds and is described by the Young–Laplace equation

$$P_{gB} - P_L = \frac{2\sigma}{R_B}, \tag{6}$$

where σ and R_B are respectively the surface tension of the liquid and the bubble radius.

It is common in the literature to model the gas in the system using the ideal gas law, which only accurately predicts gas behaviour at low pressure and high temperature. The nanobubble can hold a very high pressure[1,12] at room temperature, and hence an equation of state that captures intermolecular interactions is more appropriate. In this work, the vdW gas law is adopted for the gas in the bubble,

$$\left[P_{gB} + a\left(\frac{n_{gB}}{V_{gB}}\right)^2\right][V_{gB} - bn_{gB}] = RTn_{gB}, \tag{7}$$

where a and b are vdW constants, R is the gas constant, and T is the absolute temperature. V_{gB} is the bubble volume which can be calculated from eqn (8) assuming a spherical shape:

$$V_{gB} = \frac{4}{3}\pi R_B^3. \tag{8}$$

Theoretically, eqn (5)–(8) can be used to collectively solve n_{gB}, P_{gB}, R_B and V_{gB}, provided that other parameters in these equations are prescribed. However, to reduce the total number of physical quantities and regulate their magnitude in numerical calculations, the equations are non-dimensionalized using the following definitions, with quantities carrying a bar being dimensionless.

$$P_{gB} \equiv \overline{P_{gB}}\frac{2\sigma}{V_o^{1/3}}, \quad P_L \equiv \overline{P_L}\frac{2\sigma}{V_o^{1/3}}, \quad R_B \equiv \overline{R_B}V_o^{1/3}, \quad V_{gB} \equiv \overline{V_{gB}}V_o, \tag{9}$$

where $V_o \equiv v_{gL}N_A$. Based on this normalization, eqn (5) becomes

$$n_{gB} + \overline{kP_{gB}}(n_{gT} - n_{gB} + \tau) = n_{gT}, \tag{10}$$

where

$$\overline{k} = 2\sigma V_o^{2/3}k, \quad \tau = n_L\frac{v_L}{v_{gL}}. \tag{11}$$

Likewise, eqn (6) and (8) can be recast as

$$\overline{P_{gB}} - \overline{P_L} = \frac{1}{\overline{R_B}}, \tag{12}$$

$$\overline{V_{gB}} = \frac{4}{3}\pi\overline{R_B}^3, \tag{13}$$

while eqn (7) can be simplified to

$$\left[\overline{P_{gB}} + \overline{a}\left(\frac{n_{gB}}{\overline{V_{gB}}}\right)^2\right]\left[\overline{V_{gB}} - \overline{b}n_{gB}\right] = \lambda n_{gB}, \tag{14}$$

where

$$\overline{a} = \frac{a}{2\sigma V_o^{5/3}}, \quad \overline{b} = \frac{b}{V_o}, \quad \lambda = \frac{RT}{2\sigma V_o^{2/3}}. \tag{15}$$

For the purpose of comparison and emphasizing the importance of a good gas model, the results for ideal gas will be obtained by setting the vdW constants $\overline{a} = \overline{b} = 0$ in eqn (14), leading to

$$\overline{P_{gB}}\,\overline{V_{gB}} = \lambda n_{gB}. \tag{16}$$

Fig. 2 shows the flowchart to establish a relationship between the normalized nanobubble radius $\overline{R_B}$ and the amount of gas in the system, n_{gT}. Rather than specifying n_{gT} and solving for $\overline{R_B}$, which is numerically more challenging, the strategy here is to specify $\overline{R_B}$ and solve the corresponding n_{gT}. With a given $\overline{R_B}$, the normalized gas pressure ($\overline{P_{gB}}$) and volume ($\overline{V_{gB}}$) can be

calculated directly using eqn (12) and (13), for a specified liquid pressure ($\overline{P_L}$). Next, parallel paths are taken to calculate n_{gB} via eqn (14) and (16), respectively for the vdW and ideal gases. The determined n_{gB} value is then fed into eqn (10) to calculate n_{gT}. This process is repeated for a range of $\overline{R_B}$, establishing its relationship with n_{gT}. Other relationships can be easily determined based on $\overline{R_B}$ vs. n_{gT}, e.g., between R_B and c_{gL}. In Experimental settings, it is often not possible to separately measure the amount of gas in the bubbles and that in the liquid. Alternatively, the total mass concentration of the gas in the system (in g L^{-1}) can be calculated from the aforementioned quantities by

$$C_{gT} = \frac{n_{gT}M_g}{V_L}, \tag{17}$$

where M_g is the molecular weight of the gas. Table 3 summarizes all the parameters used in the thermodynamic modelling, their normalization, and prescribed values for the examples to be shown later.

2.2. Molecular dynamics

Molecular dynamics simulations are conducted, following a structured workflow that includes three main steps: selecting forcefields, designing the simulation systems, and defining system settings. These steps are described in detail below,
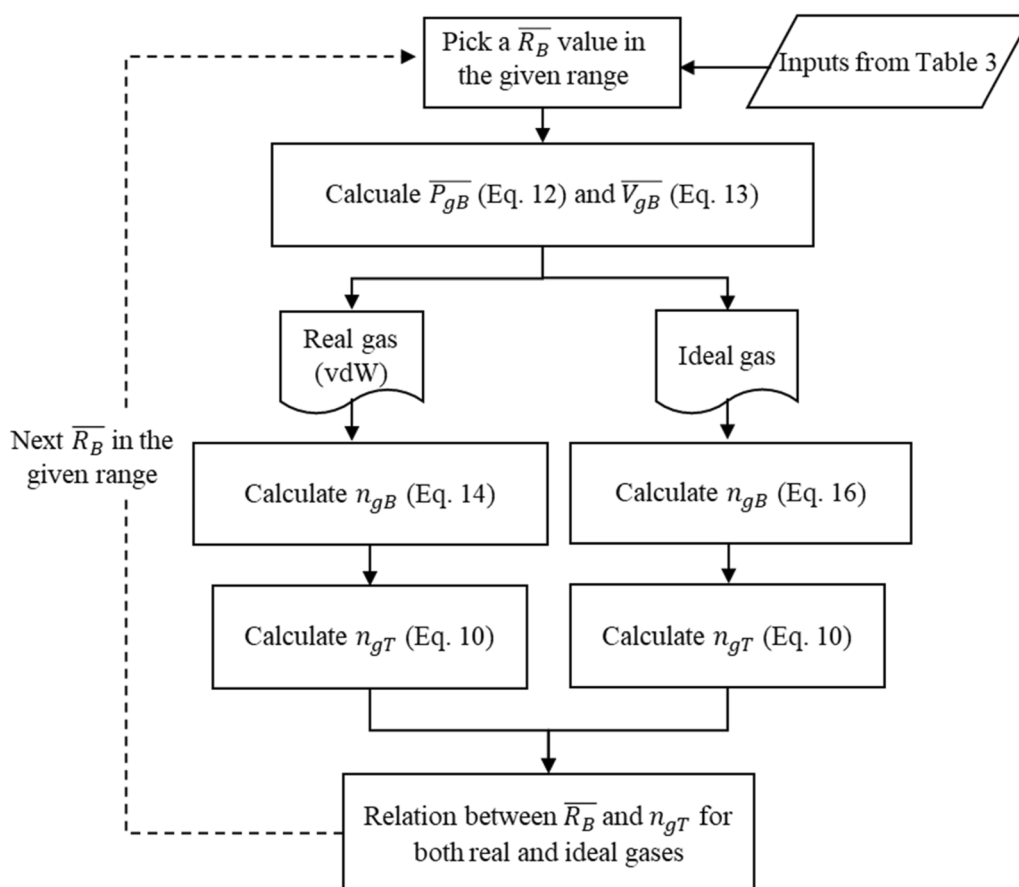

Fig. 2 Flowchart to determine the relationship between normalized bubble radius $\overline{R_B}$ and total moles of gas, n_{gT}, in the system.

Table 3 Parameters in thermodynamic modelling with normalization and prescribed values if applicable

Parameter	Definition	Prescribed or solved?	Prescribed value	Normalization
R	Gas constant	Prescribed	8.314 J mol^{-1} K^{-1}	N/A
N_A	Avogadro's number	Prescribed	6.022×10^{22} mol^{-1}	N/A
k	Henry's constant	Prescribed	7.8×10^{-4} mol L^{-1} atm^{-1} for H$_2$	$\bar{k} = 2kV_o^{2/3}$
a	vdW constant	Prescribed	17.2577 L^2 kPa mol^{-2} for H$_2$	$\bar{a} = \dfrac{a}{2\sigma V_o^{5/3}}$
b	vdW constant	Prescribed	0.0193 L mol^{-1} for H$_2$	$\bar{b} = \dfrac{b}{V_o}$
σ	Surface tension	Prescribed	72 mN m^{-1} for water	N/A
v_{gL}	Volume occupied by one gas molecule dispersed in the liquid	Prescribed	1.13×10^{-29} m^3 for H$_2$	N/A
v_L	Volume occupied by one liquid molecule	Prescribed	3.07×10^{-29} m^3 for H$_2$O	N/A
P_L	Pressure in the liquid	Prescribed	1 bar	$\overline{P_L} = \dfrac{P_L V_o^{1/3}}{2\sigma}$
T	Temperature	Prescribed	300 K	N/A
n_L	Mole of liquid (water)	Prescribed	4.98×10^{-21} to 5.5×10^{-5} mol	N/A
R_B	Bubble radius	Prescribed	0.1–10^7 nm	$\overline{R_B} = \dfrac{R_B}{V_o^{1/3}}$
n_{gB}	Mole of gas in the bubble	Solved	N/A	N/A
n_{gL}	Mole of gas in the liquid	Solved	N/A	N/A
n_{gT}	Total mole of gas in the system	Solved	N/A	N/A
P_{gB}	Pressure inside the nanobubble	Solved	N/A	$\overline{P_{gB}} = \dfrac{P_{gB} V_o^{1/3}}{2\sigma}$
V_{gB}	Volume of gas bubble	Solved	N/A	$\overline{V_{gB}} = \dfrac{V_{gB}}{V_o}$
V_L	Liquid volume	Solved	N/A	N/A
c_{gL}	Molar gas concentration in liquid	Solved	N/A	N/A
C_{gT}	Total mass concentration of gas	Solved	N/A	N/A

followed by the post-processing calculations applied to analyze the simulation outputs and relate them to thermodynamic modelling.

2.2.1. Forcefield selection. Water is chosen as the liquid phase and among the available water models, the SPC/E, TIP4P/Ew, and TIP4P/2005 models exhibit strong agreement with experiments on surface tension. To the best of our knowledge, TIP4P/2005 provides the highest accuracy, as reported by Vega *et al.*[34] Hydrogen is selected as the gas in the simulations. Tsimpanogiannis *et al.*[35] evaluated various hydrogen forcefields in the presence of water with the TIP4P/2005 forcefield, and identified the Buch forcefield[36] as the most reliable for predicting hydrogen behaviour. Guided by these findings, we adopted the TIP4P/2005 water model and the Buch forcefield for hydrogen. The accuracy of the forcefields is further confirmed by comparing the gas density of stable hydrogen bubble obtained in MD simulation with density reported for hydrogen at the same temperature and pressure in the NIST database (see SI).

2.2.2. System design and simulation setting. All MD simulations are performed using the GROMACS 2023 package.[37] Two types of closed systems are designed: pure hydrogen (Fig. 1(b)) and hydrogen–water (Fig. 1(c)).

The pure hydrogen system is simulated to extract the vdW gas constants required in the thermodynamic modelling. In these simulations, the number of hydrogen molecules remains constant (500), while pressure and temperature are varied

across a specified range: temperature (200, 250, 300, 325, 400 K), pressure (0.1, 5, 7.5, 10, 15, 20, 25, 30, 35 bar). Arbitrary combinations of these temperature and pressure values lead to a total of 45 simulations. Each simulation starts with a cubic box (initial side length of 3 nm), and undergoes three steps:

Table 4 Hydrogen–water systems designed for MD simulation. S: small system with 3000 water molecules, M: medium system with 6000 water molecules, I: intermediate system with 9000 water molecules and L: large system with 12 000 water molecules

System	#H$_2$O	#H$_2$	C_{gT} (g L^{-1})	Supersaturation	Initial box side length (nm)
S1	3000	175	6.53	4157.89	5
S2	3000	200	7.46	4751.88	
S3	3000	225	8.39	5345.86	
S4	3000	250	9.33	5939.85	
M1	6000	300	5.60	3563.91	6
M2	6000	350	6.53	4157.89	
M3	6000	400	7.46	4751.88	
M4	6000	450	8.39	5345.86	
I1	9000	450	5.60	3563.91	7
I2	9000	525	6.53	4157.89	
I3	9000	600	7.46	4751.88	
I4	9000	675	8.39	5345.86	
L1	12 000	600	5.60	3563.91	7.5
L2	12 000	700	6.53	4157.89	
L3	12 000	800	7.46	4751.88	
L4	12 000	900	8.39	5345.86	

minimization, NVT/NPT equilibration and NPT production run. The simulation begins with energy minimization using the steepest descent algorithm to stabilize the system and reduce the maximum force in the system to below 100 kJ mol^{-1} nm^{-1}. The second step is equilibration under the NVT ensemble for 1.5 ns to adjust the temperature, followed by equilibration under the NPT ensemble for 10 ns to stabilize the system and reach the target temperature and pressure. Once equilibration is completed, a 10 ns production run under NPT is performed to collect data. Temperature control is achieved using the V-rescale thermostat with coupling time constant of 0.1 ps. Pressure is maintained using the C-rescale barostat with coupling time constant of 2 ps. System compressibility is set to 3×10^{-3} bar^{-1} following the data from NIST.[33] Periodic boundary condition is applied in all three directions to mimic infinite bulk behaviour and eliminate edge effects. The cut-off radius for short-range non-bonded interactions is set to 1.2 nm. Since the hydrogen beads in the Buch forcefield have zero charge, there are no electrostatic interactions. The leap-frog integrator with 1 fs time step is used to solve the equations of motion.

The second set of systems containing both hydrogen and water are designed to study bubble dynamics across a range of hydrogen concentrations. Four distinct system sizes of small (3000 water molecules), medium (6000 water molecules), intermediate (9000 water molecules) and large (12 000 water molecules) are considered each with four different hydrogen concentrations (Table 4). The hydrogen molecules are initially randomly dispersed in the water box using the Packmol package,[38] which ensures optimal spatial distribution of molecules within the simulation box while avoiding overlaps. Table 4 also shows the initial box dimension for each system. The determination of C_{gT} and supersaturation follows the same method specified in the footnote of Table 1, with the saturation concentration of $H_2 = 0.00157$ g L^{-1}, extracted from NIST data.[33] This calculation of C_{gT} is consistent with the definition in eqn (17) for the thermodynamic model, provided that the volume of dissolved gas is much smaller than the volume of the liquid.

Each hydrogen–water system is first subjected to energy minimization using the steepest descent algorithm, to reduce the forces below 100 kJ mol^{-1} nm^{-1}. Equilibration is then conducted using the NPT ensemble for 20 ns with a Nose–Hoover thermostat and a Parrinello–Rahman barostat, controlling the system's temperature and pressure at 300 K and 1 bar, respectively. The subsequent production phase, 80 ns for data collection under the NPT ensemble, uses the same thermostat and barostat. Bond constraints for water molecules are applied using the LINCS algorithm. Periodic boundary conditions are applied in all three dimensions, and short-range non-bonded interactions are cut off at 1.2 nm. Long-range electrostatic interactions are handled using the Particle Mesh Ewald (PME) method. The leap-frog integrator is used to solve the equations of motion with a 2 fs time step. Trajectories are saved every 100 ps for post-simulation analysis. Equilibrium indicators (*e.g.*, energy and pressure fluctuations), are evaluated using built-in GROMACS tools.

2.2.3. Analysis of MD results. In the pure hydrogen simulations, the final hydrogen density is extracted for each combination of temperature and pressure. The Nelder–Mead optimization algorithm is applied to fit the vdW equation of state to the MD data and obtain the a and b values that minimize the discrepancy. This step is critical to ensure the thermodynamic properties of hydrogen are accurately represented in the hydrogen–water systems.

Bubble size in the hydrogen–water systems is determined by first detecting the nanobubbles. A distance-based criterion, derived from the radial distribution function (RDF), is introduced to identify the nanobubbles. Fig. 3 shows the RDF between hydrogen molecules for two systems of M2 and L4, representing the fundamental characteristics of all systems. A prominent peak in the RDF is observed between 0.2 and 0.6 nm, which corresponds to the close packing of hydrogen molecules within a nanobubble. The distance of 0.6 nm is therefore selected within which two hydrogen molecules are considered to be in the same nanobubble. Custom Python scripts,[39] built on the MD analysis library,[40] complement this analysis by visualizing and validating nanobubble formation. Once the nanobubbles are detected, the radius (R_B) of each nanobubble is calculated based on its gyration radius (R_G). Specifically, by approximating each nanobubble as a sphere, R_B and R_G are related by

$$R_B = R_G \times \sqrt{5/3} \qquad (18)$$

The calculated R_B is substituted into eqn (8) to calculate the bubble volume, V_{gB}. Attempt is also made to compute V_{gB} by approximating the nanobubble as an ellipsoid, leading to $V_{gB} = 4/3\pi \sqrt{5^3 \lambda_1 \lambda_2 \lambda_3}$, where $(\lambda_1, \lambda_2, \lambda_3)$ are the principal moments of the gyration tensor. Comparison between the two approaches shows less than 3% difference, confirming the validity of the spherical nanobubble assumption.
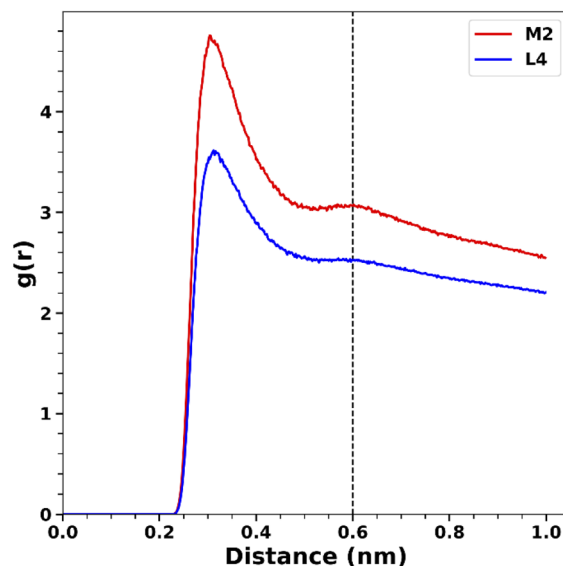

Fig. 3 Radial distribution function between hydrogen molecules for two systems of M2 and L4 showing 0.6 nm as the upper limit to consider hydrogen molecules in the same nanobubble. Pressure = 1 bar and temperature = 300 K.

3. Results

3.1. Extracting van der Waals constants from MD simulations

The Nelder–Mead algorithm is used to iteratively determine the vdW constants a and b, based on initial guesses adopted from experimental values reported for hydrogen: $a = 24$ L^2 kPa mol^{-2} and $b = 0.01$ L mol^{-1}. The optimization renders $a = 17.2577$ L^2 kPa mol^{-2} and $b = 0.0193$ L mol^{-1}. Fig. 4 shows the good agreement between the MD-calculated hydrogen density, the fit to the vdW equation of state, and the density reported from NIST database.[33]

3.2. Existence of minimum supersaturation for bubble formation

Our investigation begins with the S systems presented in Table 4. At low hydrogen concentrations (simulations are also conducted for 50, 75, 125 and 150 hydrogen molecules in addition to those listed in Table 4), the initially dissolved molecules remain dispersed throughout the simulation. However, as the concentration increases, clusters begin to form, eventually resulting in a stable nanobubble when the number of H$_2$ molecules reaches 200. At this critical concentration ($C_{gT} = 7.46$ g L^{-1}) the bubble persists throughout the simulation timeframe. Simulations with 225 and 250 hydrogen molecules are then performed to provide three data points for this system size. A similar approach is used for system sizes of M, I and L, presented in Table 4, and a concentration of 6.53 g L^{-1} is identified as the threshold above which stable nanobubbles exist for these systems.

3.3. Validity of Young–Laplace equation

In continuum theory, surface tension is considered size-independent. However, at the nanoscale, surface tension may

Fig. 4 Comparison of the pure hydrogen density from MD simulations (filled shapes), NIST data (hollow shapes), and fitting using the vdW equation of state (dashed lines).

exhibit deviations from its macroscopic counterpart, raising questions about the applicability of the Young–Laplace equation in this regime.[41] To investigate this effect, the internal pressure, P_{gB}, of each nanobubble is calculated from its volume using the vdW equation of state (eqn (7)), with a and b values derived from MD simulations (Section 3.1). This should be recognized as an approximation (although more realistic than the ideal gas model used in many studies), since the gas inside a nanobubble is not uniformly distributed, and strictly speaking pressure inside the nanobubble is a position-dependent property. The pressure difference across the hydrogen–water interface, ΔP, is then computed as $\Delta P = P_{gB} - P_L$, where $P_L = 1$ bar. ΔP is plotted against $1/R_B$ for all systems in Fig. 5. For each system, all data during the last 25 ns of the simulations are shown by scattered point and represented by a distinct marker type and color. The variability in the data is due to the dynamic nature of the nanobubble where the hydrogen molecules in the bubble can exchange with those in the bulk liquid. The pressure and bubble radius averaged from all the data are obtained for each system and shown with a hollow symbol in Fig. 5. The averaged data reveal a linear trend with little deviation from the black dash line plotted using the Young–Laplace equation (eqn (6)) and $\sigma = 72.0$ mN m^{-1}. An attempt is also made to fit the data using the Tolman correction:[41]

$$\Delta P = \frac{2\sigma_\infty}{R_B}\left(1 - \frac{\delta}{R_B}\right) \qquad (19)$$

where $\sigma_\infty = 72.0$ mN m^{-1} is the macroscopic surface tension and δ is the Tolman length. This analysis yields a Tolman length of $\delta = 0.9$ Å, more than one order of magnitude smaller than the bubble radii. Given this small value, the results indicate that the effect of curvature on surface tension is negligible. Consequently, the Young–Laplace equation with nanobubble pressure approximated from vdW equation of state holds remarkably well at the nanoscale.

3.4. Prediction of bubble size

Using the thermodynamic model established in Section 2.1, the nanobubble radius (R_B) is calculated as a function of C_{gT} and the analytical predictions are plotted in Fig. 6 for systems with different amount of water using either solid (assuming vdW gas) or dashed (assuming ideal gas) lines. Average R_B from the last 25 ns of the MD trajectory is shown in the same figure, along with the corresponding standard deviation. The results reveal a nearly perfect alignment between the simulation data and the theoretical predictions based on the vdW equation of state (solid lines). While the theoretical predictions based on the ideal gas model (dashed lines) deviate significantly from the simulation data. This comparison underscores the robustness of the framework in predicting nanobubble size when intermolecular interactions are taken into account. Notably, solving bubble size using the numerical scheme in Fig. 2 is highly efficient, without the computational expense of simulating each molecular system individually.

An important observation in Fig. 6 is the absence of simulation data on the lower branch of the theoretical curves. For the
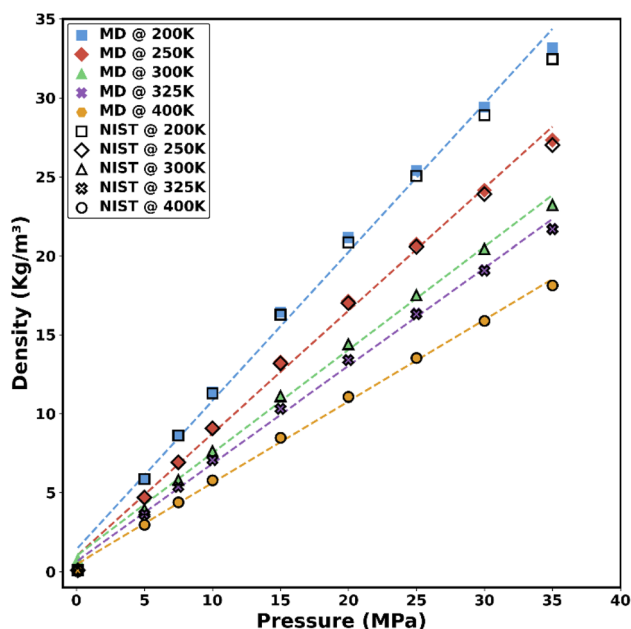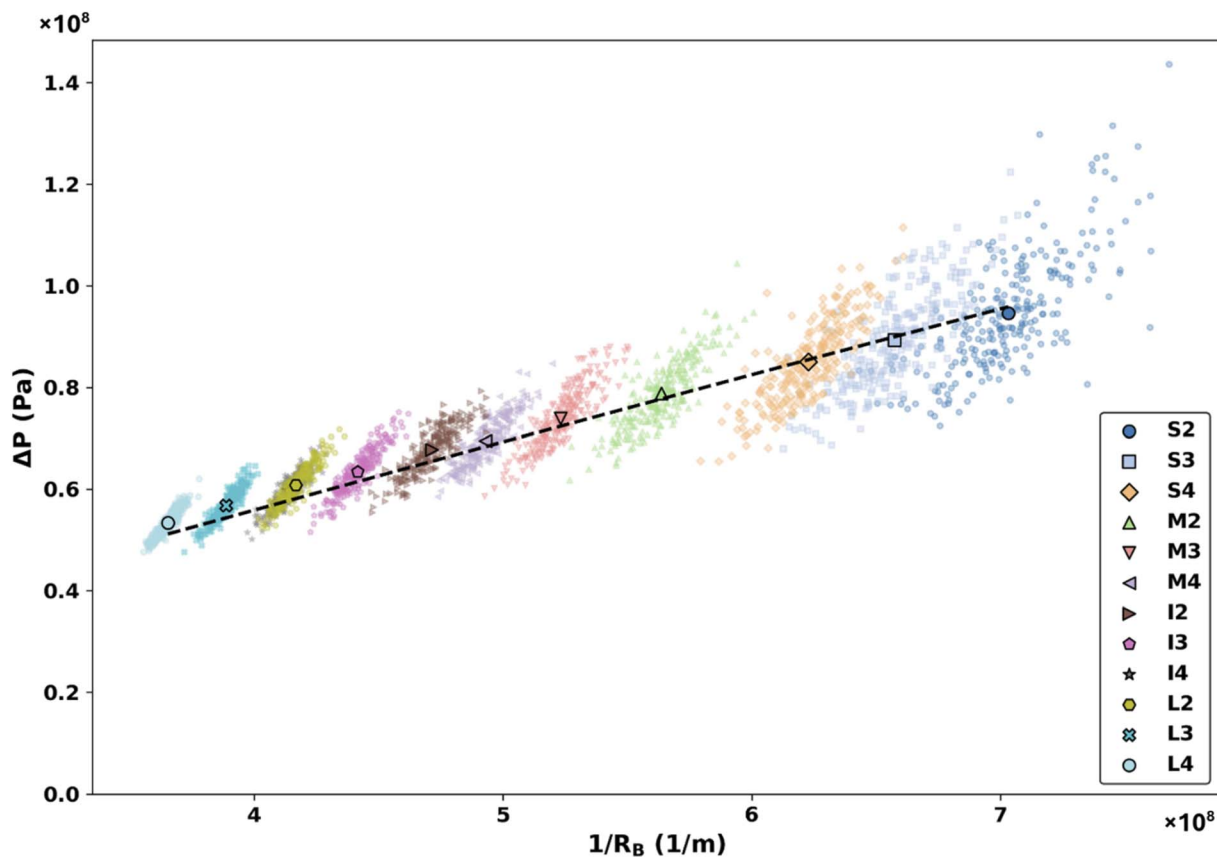
Fig. 5 The pressure difference (ΔP) as a function of $1/R_B$ for various systems studied in this work. Each colour corresponds to a different system, and the average value is shown with a hollow distinct shape. The black dashed line represents a linear fit to the data, using the Young–Laplace equation and a surface tension of 72 mN m^{-1}.

range of hydrogen concentrations studied in our MD simulations, this branch corresponds to nanobubbles with radii between 2.5 and 3.4 Å. Such radii represent minuscule clusters containing only 2–3 hydrogen molecules, which lack the cohesive interactions required for stability, leading to rapid dissolution into the bulk liquid.

3.5.   Comparison with experiments

Before our attempt to make a comparison with existing experiments in the literature, it is acknowledged that while our model predicts the size of a single nanobubble, in an experimental setup there is usually a distribution of nanobubbles which can co-exist with larger bubbles due to the more complex experimental conditions. It is hence extremely difficult to isolate a single bubble in experiments for direct comparison. However, it is possible to consider the model prediction as a representative nanobubble size in the experimental system, mimicking the situation where individual nanobubbles are not strongly interacting with each other.

In one set of experiments by Michailidi et al.,[13] air and oxygen nanobubbles were generated using a low-energy nanobubble generator based on hydrodynamic cavitation. Their setup operated under an elevated pressure of approximately 3 bar (≈ 3 atm), and the nanobubble size distribution was

determined using dynamic light scattering (DLS) along with stability analyses via ζ-potential and free radical measurements. In a separate study by Wang et al.,[42] nanobubbles containing N_2, O_2, and CO_2 were produced by a periodic pressure change device. The device first pre-saturated the solution with gas and then induced pressure fluctuations—where the pressure in the U-tube was observed to increase by roughly 0.8 atm above the ambient (≈ 1 atm), yielding an effective pressure of about 1.8 atm during the pressurization phase.

The above experimental reports did not specify the gas concentrations in their systems. To enable the comparison of experimental results with our theoretical model, the best we can do based on the provided data is to estimate the molar concentrations of dissolved gas in water (c_{gL}) using Henry's law, eqn (2). Then, the nanobubble radii under the same c_{gL} are predicted from our analytical framework. The Henry's constants are adopted from the literature as follows: O_2: 1.3×10^{-5}, N_2: 6.4×10^{-6}, air: 7.8×10^{-6}, and CO_2: 3.4×10^{-4} mol m^{-3} Pa^{-1}.[33] The volume of the liquid chamber in Michailidi et al.[13] was 4 L and that in Wang et al.[42] was 3 mL. These numbers are used to obtain n_L required by the model. The analytical predictions are compared with experimental measurements in Fig. 7, which shows a systematic discrepancy: the analytical model yields larger bubble radii than those observed experimentally. To
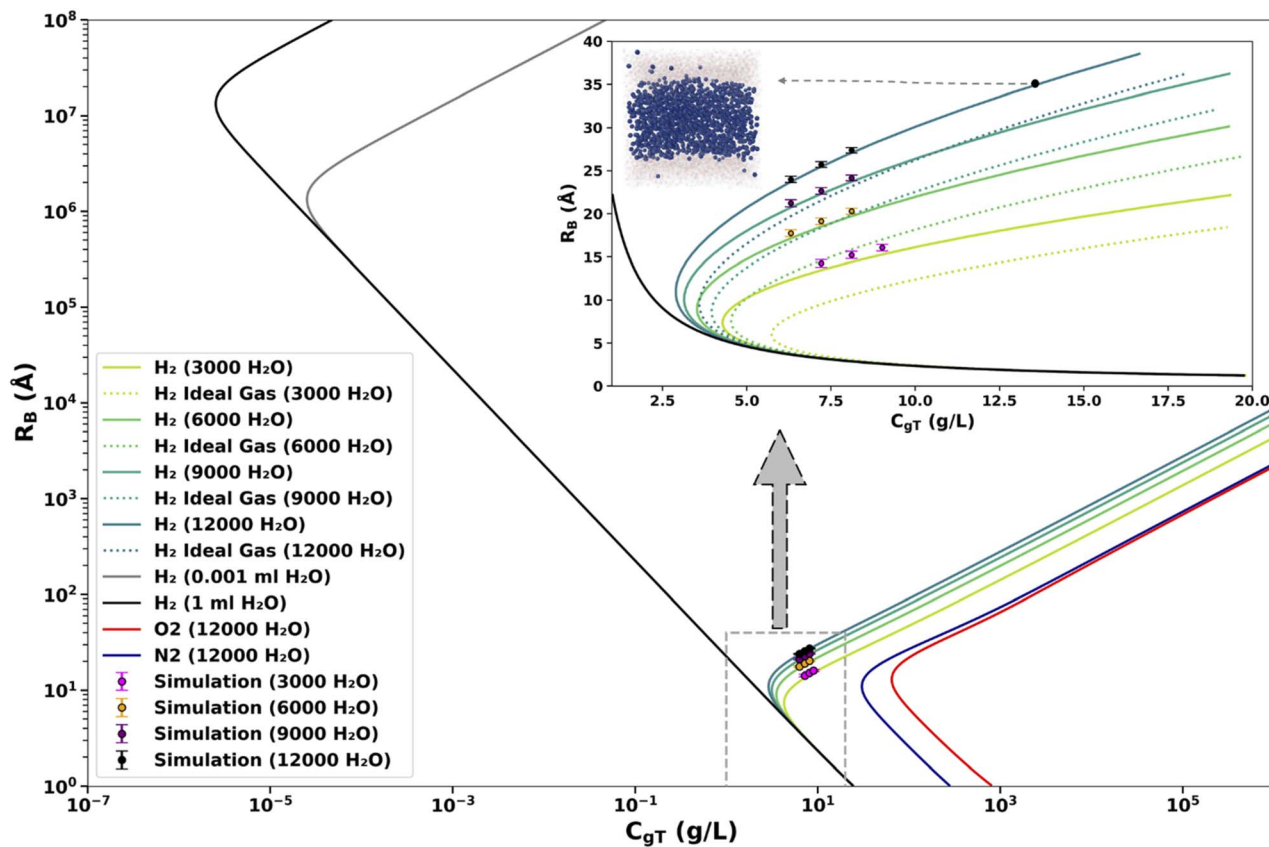
Fig. 6 Nanobubble radius (R_B) vs. total mass concentration of gas (C_{gT}), obtained from thermodynamic modelling (curves) and MD simulation (symbols).
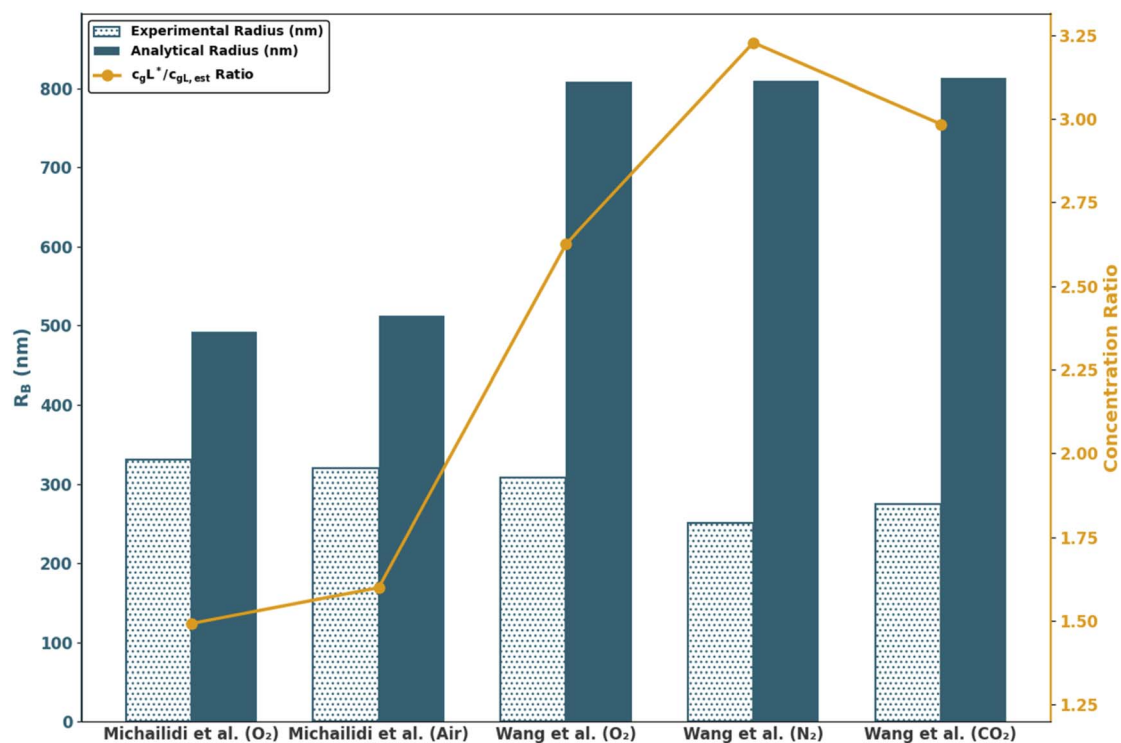

Fig. 7 Comparing experimental results with analytical predictions from this study.

quantify this deviation, we introduce a ratio $c_{gL}^*/c_{gL,est}$, where c_{gL}^* is the effective gas concentration required in our model to match the experimentally observed nanobubble radius, and $c_{gL,est}$ is the concentration estimated using Henry's law. As shown in Fig. 7, this ratio is greater than one in all cases. For example, in the study by Michailidi et al.,[13] the analytical and experimental radii converge when the effective concentration is about 1.6 times $c_{gL,est}$. This is likely because Henry's law assumes ideal, equilibrium conditions, whereas experimental systems are subject to dynamic mixing and local non-equilibrium effects that may result in higher effective concentrations of dissolved gas.

Another source of discrepancy is the time over which the experimental observations are made. Michailidi et al.[13] observed that the nanobubble size increased by approximately 1.5 times after 3 months compared to its initial size after 5 days. This temporal evolution indicates that prolonged equilibration leads to bubble growth, which may result in better agreement with the theoretical model built on strict enforcement of equilibrium. Compared to Michailidi et al.,[13] the data from Wang et al.[42] differ more from the analytical prediction, likely reflecting the shorter equilibration time reported −48 hours for N_2 and O_2, and 24 hours for CO_2—which prevented the system from reaching full equilibrium. In view of these points, better agreement is expected when parameter values in the model are made more faithful to experimental conditions. For instance, rather than applying the ideal Henry's law to estimate the dissolved gas concentrations, one could use activity/fugacity-based estimates tied to the actual gas partial pressures and the true mixture composition (air as $O_2/N_2/CO_2$ rather than a single-component proxy). An effective γ may be adopted to reflect interfacial conditions present in the measurements (e.g., ionic strength, surface-active species, and dynamic changes in interfacial tension).

Despite these deviations, the overall agreement between the analytical predictions and experimental data remains within a reasonable range, underscoring the robustness and adaptability of our framework when extrapolated to larger systems.

3.6. Discussion

Fig. 6 not only validates our framework against MD simulations but also reveals interesting behaviour when extended to larger volumes. For each system size—from the smallest 1.25×10^{-19} ml (MD simulation box containing 3000 molecules) to a hypothetical 1 ml volume—the analytical solution yields two mathematical branches. In MD simulation, only the upper branch corresponds to a stable nanobubble. The lower branch, which would imply radii of just a few angstroms, is thermodynamically unfavourable and the nanobubble disappears rapidly through dissolution. As system size grows, both branches move upwards. For the 0.001 and 1 ml systems shown in Fig. 6, the lower branch occupies a region that could, in principle, host equilibrium bubbles on the order of tens to hundreds of nanometres, while the upper branch corresponds to unrealistically large radii on the order of mm to cm. Therefore, for large systems, it is expected that the lower branch would provide

predictions that better align with experiments. Another interesting observation from Fig. 6 is that once the lower branch becomes physically accessible, its predicted radii for different system sizes collapse onto a single curve. This is in contrast to the separation of the upper branches which are physically realistic for small systems. Therefore, in large systems, equilibrium bubble size depends solely on the gas concentration and not on the liquid volume, while in small systems, liquid volume impacts bubble size, in agreement with findings previously reported in the literature.[21,29]

The sharp "elbow" in each analytical curve of Fig. 6 marks the minimum gas concentration (C_{gT}) required for a bubble to be in equilibrium. Below this concentration, the thermodynamic model has no real solution for R_B, suggesting that gas remains dispersed rather than forming a bubble. As system volume increases, we observe that the minimum C_{gT} steadily decreases which means larger liquid reservoirs require a lower degree of supersaturation to overcome the Laplace pressure barrier. This negative correlation between the critical concentration and system size is confirmed in our MD simulations: the smallest (S) systems exhibit a threshold near 7.5 g L^{-1}, whereas medium, intermediate, and large systems all transition around 6.5 g L^{-1}. Such a trend has also been reported in previous computational studies[21,24]—for example, Park et al. (2001) observed stable bubbles at lower supersaturations for larger simulation cells.[24]

Despite the overall agreement in trend, the MD-derived thresholds lie substantially above the analytical predictions—for instance, our large systems (containing 12 000 water molecules) yield a minimum C_{gT} of ~6.5 g L^{-1} in MD versus ~2.8 g L^{-1} analytically. Several effects contribute to this gap. First, the thermodynamic model assumes a perfectly smooth, spherical interface with a constant macroscopic surface tension, whereas in molecular simulations the bubble surface has rough edges, and it is not perfectly spherical—both of which can increase the local Laplace pressure and raise the barrier for bubble equilibration. Second, Henry's law is used to relate dissolved gas concentration to bubble pressure which, strictly speaking, only applies to ideal dilute solutions. Therefore, at high supersaturations, the thermodynamic model may underestimate the dissolved (and hence the total) gas concentration when an equilibrium bubble is present. Finally, finite-size and periodic-boundary effects in MD can introduce interactions between periodic images, and hinder nanobubble stabilization.

While our primary focus is hydrogen-based nanobubbles due to their importance in various applications, the methodology is broadly applicable to nanobubbles formed by other gases. When we substitute nitrogen or oxygen for hydrogen in the large system (12 000 water molecules), the same two-branch trend emerge (Fig. 6), but the predicted bubble sizes shrink. At the same C_{gT}, bubble radii for the three gases follow the order of $H_2 > N_2 > O_2$.

Within the nanobubble literature, the closest research to ours was performed by Weijs et al.,[21] but with differences in three fundamental aspects. First, the bubbles were modeled as 2D cylinders in Weijs et al.[21] while we consider 3D geometry which is more realistic. Second, while Weijs et al. employed an

ideal gas description in their continuum model—focusing on diffusive shielding effects in nanobubble clusters—we explicitly incorporate non-ideal gas behavior using the vdW equation of state. This modification is critical because nanobubbles experience extremely high internal pressures, where the ideal gas law becomes inadequate. Fig. 6 shows the importance of considering the non-ideal gas law when predicting the bubble size. The third improvement is the incorporation of parameters derived at microscopic scale into a macroscopic model. These parameters include molecular volumes for the liquid and dissolved gas, v_L and v_{gL}. Under the isothermal–isobaric condition, the pressure in the liquid is prescribed while the system volume is not known *a priori*. Incorporating v_L and v_{gL} in the model removes the need for an empirical equation of state for the liquid that specifies a relationship between pressure and volume. In addition, while the vdW constants a and b can be determined using experimental sources (*e.g.*, NIST database[33]), they are calibrated in our work using MD simulation data, an approach that can be extended to any gases (in pure or mixed forms) especially when experimental data are unavailable. This integration of molecular-level details into a thermodynamic framework enhances the predictive capability of our model for the nanoscale systems studied.

It is important to recognize the practical constraints of MD simulations in exploring the full range of nanobubble behaviour. While our theoretical curves in the inset of Fig. 6 indicate that ever-larger bubbles should form as C_{gT} increases, intrinsic limitations in box size and computational cost prevent MD from reaching those regimes. For example, at $C_{gT} \approx 13.50$ g L^{-1} the model predicts a bubble radius of 34.8 Å, yet a cubic simulation cell with side length $L = 80.4$ Å cannot physically accommodate such a bubble without significant interaction between periodic images. In this example, $L - 2R_B \approx 10.8$ Å, which falls below the 12 Å cut-off distance for nonbonded interactions. Under such conditions, the bubble is artificially distorted into a cylindrical shape, as shown in the inset of Fig. 6. The thermodynamic framework, on the other hand, does not have these limitations or the high computational cost of MD, offering reliable bubble-size predictions across supersaturation levels and volumes far beyond current simulation feasibility.

As acknowledged earlier, the gas density inside a nanobubble is intrinsically non-uniform. A rigorous route for predicting the radial density profile together with the curvature-dependent interfacial tension is provided by classical density functional theory (cDFT). For example, Peng and Yu showed that cDFT can self-consistently capture non-uniform gas densities and interfacial properties at nanometre scales.[43] In contrast, the present study adopts a simplified but practical closure: the nanobubble's internal pressure is assumed to be uniform and approximated from a real-gas (vdW) equation of state whose parameters are calibrated to MD. This approach trades some microscopic details for computational efficiency and direct comparability with MD outputs. Extending our framework to a cDFT-based description of the gas phase and interface is a natural direction for future work and may further improve quantitative accuracy when strong inhomogeneities are present.

In addition, it is worth investigating whether the strong applicability of the Young–Laplace equation, discovered here for hydrogen in water, is also valid for other gas/liquid combinations or corrections for nanoscale effects might be required. Moreover, the application of Henry's law warrants careful discussion. Our MD calculations yield dissolved gas concentrations ranging 0.697–1.658 g L^{-1}, which are significantly higher than the saturation concentration (0.00157 g L^{-1} (ref. 33)), thereby violating the dilute-solution assumption underlying Henry's law. Despite this, the model appears to capture the nanobubble behavior well, both qualitatively and quantitatively. Future improvements could involve adopting a modified solubility law or incorporating non-linear concentration dependencies into the thermodynamic model, thereby providing a more accurate description of the equilibrium states in supersaturated systems.

4. Conclusions

An integrated framework is developed that synergistically combines molecular dynamics (MD) simulations of pure gases with a van der Waals gas-based thermodynamic model to predict the equilibrium size of nanobubbles in supersaturated liquid. Our results indicate that equilibrium bulk nanobubbles emerge only when the gas concentration exceeds a critical threshold, below which bubble formation is thermodynamically unfavored. The Young–Laplace equation, with nanobubble pressure approximated from the van der Waals equation of state, effectively captures the interfacial pressure jump even at radii as small as a few nanometers, without the need for Tolman correction. The van der Waals constants tuned to the MD data enable this framework to reproduce nanobubble radii observed in hydrogen–water simulations with significantly reduced computational overhead. The comparison between theory and simulation highlights the importance of considering intermolecular interactions when the gas is under ultra-high pressure inside a nanobubble. Henry's law, although originally formulated for dilute solutions, can still offer a reasonable baseline for modelling gas solubility in nanoscale contexts. Overall, this work underscores the robustness and flexibility of uniting molecular and continuum descriptions to investigate nanobubbles. Future research could integrate effects such as dynamic gas exchange, external fields, and interfacial charge to address a broader array of conditions with potential applications across energy, biotechnology, and soft matter systems.

Author contributions

Ali Ghamartale: conceptualization, data curation, formal analysis, investigation, methodology, software, validation, visualization, writing – original draft. Ehsan Shahini: data curation, formal analysis, investigation, methodology, software, validation, visualization, writing – original draft. Aditya Jain: data curation, investigation, methodology, software. Rogerio Manica: conceptualization, writing – review & editing. Peter Berg: conceptualization, formal analysis, project administration, supervision, writing – review & editing. Tian Tang:

conceptualization, formal analysis, funding acquisition, methodology, project administration, resources, supervision, writing – review & editing.

Conflicts of interest

There are no conflicts to declare.

Data availability

Data for this article will be made available upon request.

Supplementary information (SI): forcefield verification using nanobubble density analysis. See DOI: **https://doi.org/10.1039/d5ra07908j**.

Acknowledgements

References

1 A. W. Foudas, R. I. Kosheleva, E. P. Favvas, M. Kostoglou, A. C. Mitropoulos and G. Z. Kyzas, *Chem. Eng. Res. Des.*, 2023, **189**, 64–86.

2 J. Lei, D. Huang, W. Zhao, S. Liu and Y. Yue, *Int. J. Heat Mass Transfer*, 2024, **225**, 125407.

3 G. S. Manning, *Phys. Chem. Chem. Phys.*, 2020, **22**, 17523–17531.

4 E. D. Michailidi, G. Bomis, A. Varoutoglou, E. K. Efthimiadou, A. C. Mitropoulos and E. P. Favvas, in *Interface science and technology*, Elsevier, 2019, vol. 30, pp. 69–99.

5 H. Bao, Y. Zhang, S. Lv, S. Liu and W. Fan, *Environ. Int.*, 2024, 109126.

6 S. Wang, Y. Liu, T. Lyu, G. Pan and P. Li, *ACS ES&T Water*, 2020, **1**, 376–387.

7 M. Soltani, F. M. Kashkooli, M. A. Fini, D. Gharapetian, J. Nathwani and M. B. Dusseault, *Renewable Sustainable Energy Rev.*, 2022, **167**, 112729.

8 Y. Tanaka and N. Miwa, *Hydrogen*, 2022, **3**, 161–178.

9 I. Ohsawa, M. Ishikawa, K. Takahashi, M. Watanabe, K. Nishimaki, K. Yamagata, K.-i. Katsura, Y. Katayama, S. Asoh and S. Ohta, *Nat. Med.*, 2007, **13**, 688–694.

10 A. Angulo, P. van der Linde, H. Gardeniers, M. Modestino and D. F. Rivas, *Joule*, 2020, **4**, 555–579.

11 M. Blander and J. L. Katz, *AIChE J.*, 1975, **21**, 833–848.

12 S. A. Hewage and J. N. Meegoda, *Colloids Surf., A*, 2022, **650**, 129565.

13 E. D. Michailidi, G. Bomis, A. Varoutoglou, G. Z. Kyzas, G. Mitrikas, A. C. Mitropoulos, E. K. Efthimiadou and E. P. Favvas, *J. Colloid Interface Sci.*, 2020, **564**, 371–380.

14 K. Ohgaki, N. Q. Khanh, Y. Joden, A. Tsuji and T. Nakagawa, *Chem. Eng. Sci.*, 2010, **65**, 1296–1300.

15 L. Zhou, S. Wang, L. Zhang and J. Hu, *Curr. Opin. Colloid Interface Sci.*, 2021, **53**, 101439.

16 B. H. Tan, H. An and C.-D. Ohl, *Phys. Rev. Lett.*, 2020, **124**, 134503.

17 F. Eklund, M. Alheshibri and J. Swenson, *Curr. Opin. Colloid Interface Sci.*, 2021, **53**, 101427.

18 M. R. Ghaani, P. G. Kusalik and N. J. English, *Sci. Adv.*, 2020, **6**, eaaz0094.

19 Y.-X. Yu and J. Wu, *J. Chem. Phys.*, 2002, **116**, 7094–7103.

20 D. Zhou, Z. H. Ansari and J. Mi, *J. Phys.: Condens. Matter*, 2013, **25**, 184004.

21 J. H. Weijs, J. R. Seddon and D. Lohse, *ChemPhysChem*, 2012, **13**, 2197–2204.

22 Y. Zhang and D. Lohse, *J. Fluid Mech.*, 2023, **975**, R3.

23 Y. A. Perez Sirkin, E. D. Gadea, D. A. Scherlis and V. Molinero, *J. Am. Chem. Soc.*, 2019, **141**, 10801–10811.

24 S. Park, J. Weng and C. Tien, *Int. J. Heat Mass Transfer*, 2001, **44**, 1849–1856.

25 M. Matsumoto, *J. Fluid Sci. Technol.*, 2008, **3**, 922–929.

26 T. Yamamoto and S. Ohnishi, *Phys. Chem. Chem. Phys.*, 2011, **13**, 16142–16145.

27 M. Zhang, Y.-s. Tu and H.-p. Fang, *Appl. Math. Mech.*, 2013, **34**, 1433–1438.

28 S. Jain and L. Qiao, *AIP Adv.*, 2017, **7**, 045001.

29 S.-N. Hong, S.-H. Choe, U.-G. Jong, M.-S. Pak and C.-J. Yu, *Fluid Phase Equilib.*, 2019, **487**, 45–51.

30 Z. Gao, W. Wu, W. Sun and B. Wang, *Langmuir*, 2021, **37**, 11281–11291.

31 Y. Lu, L. Yang, Y. Kuang, Y. Song, J. Zhao and A. K. Sum, *Phys. Chem. Chem. Phys.*, 2021, **23**, 27533–27542.

32 A. S. Al-Awad, L. Batet, R. Rives and L. Sedano, *J. Chem. Phys.*, 2024, **161**, 024503.

33 R. Sander, *NIST Standard Reference Database*, 2017.

34 C. Vega and E. de Miguel, *J. Chem. Phys.*, 2007, **126**, 154707.

35 I. N. Tsimpanogiannis, S. Maity, A. T. Celebi and O. A. Moultos, *J. Chem. Eng. Data*, 2021, **66**, 3226–3244.

36 V. Buch, *J. Chem. Phys.*, 1994, **100**, 7610–7629.

37 M. Abraham, A. Alekseenko, C. Bergh, C. Blau, E. Briand, M. Doijade, S. Fleischmann, V. Gapsys, G. Garg, S. Gorelov, G. Gouaillardet, A. Gray, M. E. Irrgang, F. Jalalypour, J. Jordan, C. Junghans, P. Kanduri, S. Keller, C. Kutzner, J. A. Lemkul, M. Lundborg, P. Merz, V. Miletić, D. Morozov, S. Páll, R. Schulz, M. Shirts, A. Shvetsov, B. Soproni, D. v. d. Spoel, P. Turner, C. Uphoff, A. Villa, S. Wingbermühle, A. Zhmurov, P. Bauer, B. Hess and E. Lindahl, *Zenodo*, 2024, DOI: **10.5281/zenodo.11104865**.

38 L. Martínez, R. Andrade, E. G. Birgin and J. M. Martínez, *J. Comput. Chem.*, 2009, **30**, 2157–2164.

39 A. Ghamartale, S. Zendehboudi and N. Rezaei, *Energy Fuels*, 2020, **34**, 13186–13207.

40 R. J. Gowers, M. Linke, J. Barnoud, T. J. E. Reddy, M. N. Melo, S. L. Seyler, J. Domanski, D. L. Dotson, S. Buchoux and I. M. Kenney, *MDAnalysis: a Python Package for the Rapid Analysis of Molecular Dynamics Simulations*, Report 2575-9752, Los Alamos National Laboratory (LANL), Los Alamos, NM (United States), 2019.

41 R. C. Tolman, *J. Chem. Phys.*, 1949, **17**, 333–337.

42 Q. Wang, H. Zhao, N. Qi, Y. Qin, X. Zhang and Y. Li, *Sci. Rep.*, 2019, **9**, 1118.

43 B. Peng and Y.-X. Yu, *Langmuir*, 2008, **24**, 12431–12439.